Available online at www.sciencedirect.com
SCIENCE DIRECT®
Journal of Solid State Chemistry 177 (2004) 2350–2357
JOURNAL OF SOLID STATE CHEMISTRY
http://elsevier.com/locate/jssc

Phase equilibrium and electrical conductivity of $SrCo_{0.8}Fe_{0.2}O_{3-\delta}$

N. Grunbaum, L. Mogni, F. Prado,* and A. Caneiro

Centro Atómico Bariloche, CNEA, TEMADI, Av. Bustillo 9500, 8400 S. C. de Bariloche, Argentina

Received 8 December 2003; received in revised form 16 March 2004; accepted 22 March 2004

Abstract

The phase diagram of the $SrCo_{0.8}Fe_{0.2}O_{3-\delta}$ compound has been determined at high temperatures ($823 \leqslant T \leqslant 1223$ K) and in the oxygen partial pressure range ($10^{-5} \leqslant pO_2 \leqslant 1$ atm) by thermogravimetric measurements of the equilibrium pO_2, high temperature X-ray diffraction and electrical conductivity measurements. The cubic perovskite phase $SrCo_{0.8}Fe_{0.2}O_{3-\delta}$ is stable in a broad range of oxygen content, while the orthorhombic brownmillerite phase $SrCo_{0.8}Fe_{0.2}O_{2.5}$ stabilizes within a small range around $3-\delta = 2.5$ at temperatures below 1073 K. Equilibrium pO_2 measurements under isothermal conditions show chemical hysteresis at the perovskite to brownmillerite transition. The hysteresis loop decreases its amplitude in pO_2 with decreasing temperature. This behavior is discussed considering the evolution from coherent intergrowth interfaces with elastic strain energy to incoherent interfaces without elastic strain energy as T decreases. The thermodynamic quantities $h_{O_2}^{oxide}$ and $s_{O_2}^{oxide}$ for the perovskite phase decrease when increasing the oxygen defects concentration. The electrical conductivity (σ) of the cubic phase exhibits a thermally activated behavior at high temperature. The variation of σ with the oxygen content is non-linear and the activation energy varies from 0.4 to 0.28 eV as the oxygen content increases from 2.4 to 2.6. These results are interpreted in the frame of the small polaron model.
© 2004 Elsevier Inc. All rights reserved.

PACS: 72.60

Keywords: Mixed conductors; Strontium iron cobalt oxide; Phase diagram; Electrical transport

1. Introduction

After the study of Teraoka et al. [1] on the oxygen permeation properties of the perovskite oxide mixed conductors $(La, Sr)(Co, Fe)O_{3-\delta}$, the $SrCo_{0.8}Fe_{0.2}O_{3-\delta}$ compound has received much attention due to its high oxygen permeability [2–4]. The high ionic conductivities ($0.01 \leqslant \sigma_i \leqslant 1\,S\,cm^{-1}$), along with the high electronic conductivity values ($20 \leqslant \sigma_e \leqslant 2 \times 10^3\,S\,cm^{-1}$) for the temperature range $1073 \leqslant T \leqslant 1273$ K [2] make these compounds suitable for electrochemical applications such as electrodes in solid oxide fuel cells (SOFC) and oxygen separation membranes [5,6]. For example, the use of mixed conductors in oxygen separation membranes would provide a low cost method for the oxidation of methane in value added products such as methanol, formaldehyde, ethane, ethylene, and syngas [7]. In such devices the membrane separates two atmospheres with different oxygen concentration. The feed side is exposed to a gas phase rich in oxygen, while the other side is exposed to a gas phase with a low oxygen partial pressure (pO_2). The oxygen chemical potential gradient established across the membrane along with the high electronic and ionic conductivities determine the spontaneous oxygen permeation flux through the membrane according to the Wagner formula [8]. Thus, the membrane must be stable under high oxygen partial pressure gradients at high temperatures, highly reducing atmospheres and temperature cycling.

The $x = 0$ compound of the $SrCo_{1-x}Fe_xO_{3-\delta}$ solid solution crystallizes in the *R32* hexagonal symmetry [9,10]. The addition of Fe changes the hexagonal symmetry to cubic, which increases the oxygen permeability to values as high as $10^{-6}\,mol\,cm^{-2}\,s^{-1}$ at 1173 K for $x = 0.2$ [3]. The cubic or pseudo-cubic structure (C) of the $SrCo_{0.8}Fe_{0.2}O_{3-\delta}$ material [8] is stable in the temperature range $823 \geqslant T \geqslant 1173$ K for $pO_2 \geqslant 0.209$ atm where it exhibits a wide range of oxygen non-stoichiometry with $3-\delta$ values ranging between 2.43 and 2.65 [11]. In contrast, the brownmillerite phase (O) with

*Corresponding author. Fax: +54-2944-445299.
E-mail address: fprado@cab.cnea.gov.ar (F. Prado).

0022-4596/$ - see front matter © 2004 Elsevier Inc. All rights reserved.
doi:10.1016/j.jssc.2004.03.026

orthorhombic symmetry (space group *Icmm*) displays a narrow range of oxygen non-stoichiometry around 2.5. The brownmillerite phase precipitates from the cubic phase after the oxygen vacancies order along the $[101]_p$ direction in alternating (0 1 0) perovskite planes [12] producing a $\sqrt{2}a_p \times 4a_p \times \sqrt{2}a_p$ supercell. The oxygen ordering leads to a layer structure in which BO_6 octahedra alternate with BO_4 tetrahedra along the *c*-axis.

The cubic–orthorhombic transition occurring at $T < 1073$ K under a wide pO_2 range has been reported to be a disadvantage for using $SrCo_{0.8}Fe_{0.2}O_{3-\delta}$ as a ceramic membrane [4,13]. The appearance of the brownmillerite phase at the low oxygen concentration side diminishes the oxygen flux across the membranes due to a lower oxygen ion conductivity compared to the perovskite phase [4].

The compound $SrCo_{0.8}Fe_{0.2}O_{3-\delta}$ has also been tested as cathode in a SOFC based on the electrolyte $La_{0.8}Sr_{0.2}Ga_{0.83}Mg_{0.17}O_{2.81}$. The authors have reported low cathode overpotential values, but thermal expansion coefficients higher than those of the electrolyte [14].

Previous works have studied the oxygen non-stoichiometry as a function of T and pO_2 of $SrCo_{0.8}Fe_{0.2}O_{3-\delta}$ [11] and $SrCo_{1-x-y}Fe_xCr_yO_{3-\delta}$ [15,16]. In particular, Liu et al. [11] have determined by thermogravimetry measurements at constant pO_2 (isobars) the range where the cubic and orthorhombic phases coexist in the $SrCo_{0.8}Fe_{0.2}O_{3-\delta}$ compound for the pO_2 values $10^{-5} \leqslant pO_2 \leqslant 1$ atm and temperatures between 823 and 1173 K.

In the present work, we have undertaken a more detailed study of the high temperature properties of the $SrCo_{0.8}Fe_{0.2}O_{3-\delta}$ compound. The equilibrium phase diagram and the partial molar enthalpy and entropy of oxygen solution in the cubic phase, $h_{O_2}^{oxide}$ and $s_{O_2}^{oxide}$, respectively, have been evaluated from thermogravimetric data of the equilibrium pO_2, and high temperature XRD for $10^{-5} \leqslant pO_2 \leqslant 1$ atm and $823 \leqslant T \leqslant 1223$ K. Transport properties as a function of temperature and pO_2 have been determined from AC conductivity measurements.

These measurements allowed us to obtain a more detailed pO_2-T phase diagram of the $SrCo_{0.8}Fe_{0.2}O_{3-\delta}$ compound and to discuss the partial molar thermodynamic properties of the C phase and the transport properties of the C and O phases.

2. Experimental

The $SrCo_{0.8}Fe_{0.2}O_{3-\delta}$ sample was prepared following the solid state reaction method. Stoichiometric quantities of highly pure $SrCO_3$, Fe_2O_3, Co_3O_4 were weighed and then ground in a ball mill. $SrCO_3$ was heated at 500°C before use in order to eliminate absorbed and chemical bonded products. The powder was calcinated at 1223 K in air for 12 h. The final heat treatment was performed at 1423 K for a period of 12 h with an intermediate grinding.

Powder X-ray diffraction data of the as-made samples were collected in the 2θ region $10 \leqslant 2\theta \leqslant 90°$ on a Philips PW1700 diffractometer using Cu $K\alpha$ radiation and a graphite monochromator. The collection time by steps of 0.02° was 10 s. The strong peaks of the X-ray data at room temperature could be indexed on a primitive cubic unit cell corresponding to the undistorted perovskite phase (space group *Pm3m*). The presence of extra weak reflections could be explained on the basis of a crystal structure with orthorhombic symmetry at room temperature [8]. No evidence of secondary phases was detected.

For high temperature X-ray diffraction (HTXRD) the sample was spread on a resistively heated platinum ribbon mounted in an Anton Paar HTK-10 camera coupled to the diffractometer. The pO_2 within the camera was controlled by means of flowing N_2-O_2 mixtures supplied by an electrochemical system [17].

Isothermal measurements of equilibrium pO_2 and isobaric runs under constant pO_2 were performed using a highly sensitive thermogravimetric equipment [18] consisting of a symmetrical thermobalance based on a Cahn 1000 electrobalance coupled to an electrochemical gas blending system similar to that used in the high temperature X-ray camera. This electrochemical system (zirconia pump and oxygen sensor) [17] provides a controlled Ar–O_2 atmosphere for the thermobalance with pO_2 values ranging from 1 to 10^{-6} atm. The error in pO_2 in the Ar–O_2 mixtures, including systematic ones, can be estimated as 2%. The thermobalance detects changes in $3-\delta$ within 0.0005 for a sample of about 1 g of $SrCo_{0.8}Fe_{0.2}O_{3-\delta}$. The oxygen content was determined by in situ reduction in dry 10%H_2/Ar at 1273 K assuming SrO, Co and Fe as final products.

Dense samples for conductivity measurements were obtained by pressing the powder, originally calcinated at 1223 K for 12 h, into pellets and then sintering at 1423 K for 12 h in air. Conductivity measurements as a function of temperature under controlled pO_2 were carried out by a standard four-probe AC method with a lock-in amplifier on bar shaped samples. The electrical wires were attached to the sample using Ag/Pd paste on sputtered gold contacts.

3. Results and discussion

3.1. Thermogravimetry and HTXRD

Fig. 1 shows the isotherm at 1023 K obtained under reduction and subsequent oxidation of the sample. Its different parts are briefly described below.

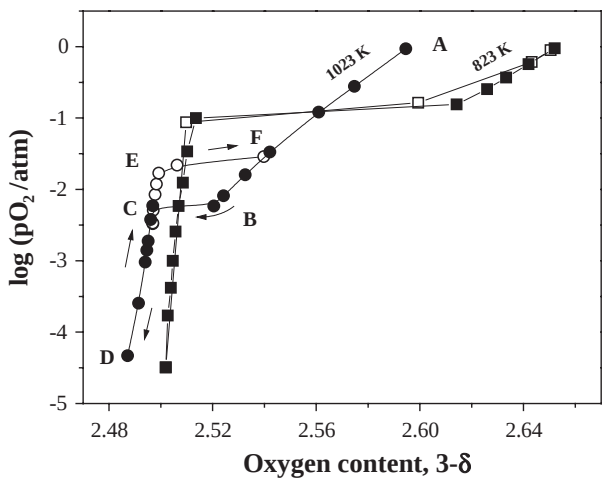

Fig. 1. Log(pO_2/atm) vs. $3-\delta$ plots at 823 and 1023 K for $SrCo_{0.8}Fe_{0.2}O_{3-\delta}$. Closed and open symbols correspond to the reduction and oxidation processes, respectively.

Parts A and B: The sample was first annealed in pure oxygen at 1023 K until equilibrium was reached (point A). Afterward, the pO_2 was decreased and equilibrium pO_2 data points between points A and B were obtained. The oxygen content of point B is $3-\delta = 2.517$ for $pO_2 = 4.1 \times 10^{-3}$ atm.

Parts B and C: When pO_2 was slightly lowered below the value corresponding to point B, the weight loss kinetics of the sample was slower than that observed for part A–B. As a consequence the equilibrium corresponding to point C was reached after two days.

Parts C–D/D–E: Point D was obtained from point C after equilibrium pO_2 was progressively lowered. Increasing pO_2 from point D, data points up to point E were obtained. The reproducibility of the oxygen content values for both increasing and decreasing pO_2 indicates thermodynamic equilibrium states.

Parts E and F: After a slight increment of pO_2 beyond point E, the sample became unstable and began to oxidize reaching point F after two days. From point F and increasing pO_2 the part F–A was reproduced. This result indicates that the A–F data points correspond to thermodynamic equilibrium states and that no evaporation of the sample took place during the measurements.

Clearly, the isotherm exhibits two regions with different behavior. Part A–B reveals the large range of oxygen non-stoichiometry of the cubic phase, while part D–E indicates the stabilization of the stoichiometric brownmillerite phase $Sr_2Co_{1.6}Fe_{0.4}O_5$.

The slow weight loss kinetics observed after decreasing pO_2 from point B indicates the precipitation of the brownmillerite phase from the perovskite. Similar behavior can be observed upon oxidation for pO_2 values slightly higher than the pO_2 value corresponding to point E. However, in this case the cubic phase precipitates from the brownmillerite phase. The large chemical hysteresis in the B–C/E–F region causes multivaluated values of pO_2 for a given oxygen content. Thus, the Gibbs rule that anticipates a unique pO_2 value for the two-phase field region cannot be applied. The hysteretic behavior in pO_2 has been extensively discussed in the literature and is associated to the existence of two phases with close compositions and related structures [19,20]. These conditions are required to create coherent interfaces or semi-coherent interfaces with low interfacial free energy and a non-negligible elastic strain energy (ΔG_s) [21]. The contribution of ΔG_s makes the Gibbs rule invalid and must be added to those of both phases in order to describe the total Gibbs energy of the system (G).

In Fig. 1 the 823 K isotherm overlapping that of the 1023 K isotherm is shown. The width of the two-phase field region increases as T decreases. This is in agreement with the two-phase field region of the T vs. $3-\delta$ diagram determined by Liu et al. [11]. On the other hand, the pO_2 amplitude of the hysteresis loop in the pO_2-composition isothermal path decreases with decreasing temperature becoming negligible for $T = 823$ K. This result rules out thermally activated processes such as cation rearrangements to explain chemical hysteresis. We believe that this behavior is related to the fact that the compositional difference (oxygen content) between both phases increases as T decreases. These compositional differences should increase the lattice misfit between both phases promoting decoherence of the coherent or semi-coherent interfaces with the consequent reduction of the elastic strain energy and consequently chemical hysteresis. The phase boundary between the cubic (C) and the two-phase field region (C + O) could not be determined univocally due to chemical hysteresis. Thus, its determination depends on the pO_2 history of the sample. For instance, under reduction this boundary corresponds to point B, while under oxidation it corresponds to point F. This uncertainty in the determination of the (C + O)/C phase boundary is measured by the difference between points F and B. The O/(C + O) phase boundary can be more accurately determined since the oxygen content values of points C and E are closer.

In Fig. 2 we show all the isotherms obtained through thermogravimetric measurements. For clarity, only equilibrium pO_2 values determined under reduction conditions are shown. These measurements indicate that the two-phase field region (C + O) disappears at $T > 1023$ K in agreement with those reported by Liu et al. [11]. The wide range of oxygen non-stoichiometry of the isotherms at $T \geqslant 1073$ K indicates that the cubic phase is stable for the whole range of pO_2. It can also be seen that the ordered phase displays a small range of oxygen non-stoichiometry. The behavior of the pO_2-$\delta-T$ curves for the oxygen content region $3-\delta < 2.5$ indicates that for pO_2 values lower than 10^{-3} atm, the C

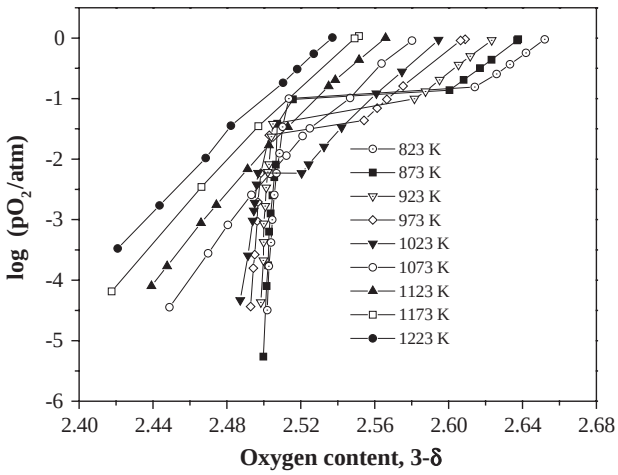

Fig. 2. Log (pO_2/atm) vs. $3-\delta$ plots for $SrCo_{0.8}Fe_{0.2}O_{3-\delta}$ at several temperatures during the reduction process.

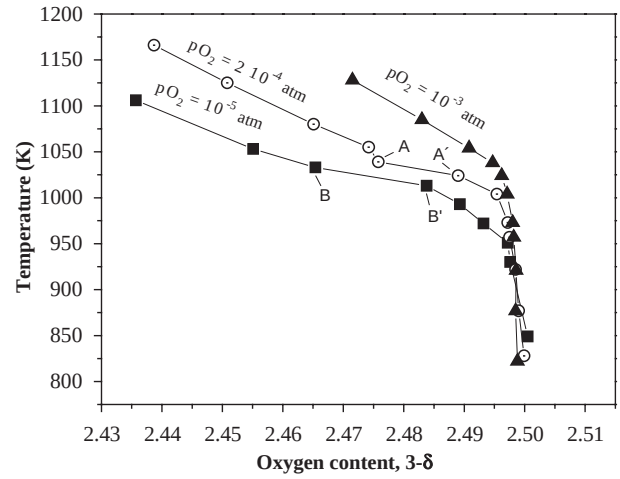

Fig. 3. Variation of the oxygen content with temperature for $SrCo_{0.8}Fe_{0.2}O_{3-\delta}$ at constant pO_2 values.

phase precipitates from the O phase when temperature increases at constant pO_2. Therefore, the temperature–composition phase diagram should also contain a two-phase field region for oxygen content values $3-\delta<2.5$. Liu et al. [11] have only determined the C + O region for oxygen content values $3-\delta>2.5$. The equilibrium pO_2 values corresponding to the coexistence of both phases in the oxygen content region $3-\delta<2.5$ are lower than those for the oxygen content region $3-\delta>2.5$. The variation of the equilibrium pO_2 for the coexistence of both phases with temperature in the range $1023\leqslant T\leqslant 1073$ seems to be very sensitive with temperature. This effect along with the slow kinetics of the sample to approach equilibrium for $pO_2\leqslant 10^{-3}$ atm hamper its determination by isothermal measurements.

An attempt at determining the two-phase field region for oxygen content values $3-\delta<2.5$ was performed through thermogravimetric measurements at constant pO_2. The temperature was changed by steps from low to high temperature while pO_2 remained constant. The equilibrium data points for three isobars are shown in Fig. 3.

The isobars obtained at $pO_2=1\times10^{-3}$, 2×10^{-4} and 1×10^{-5} atm show that the orthorhombic phase displays negligible oxygen non-stoichiometry at low temperature ($T<950$ K). At $pO_2=10^{-3}$ atm the sample begins to lose oxygen at $T>1025$ K. The variation of the oxygen content as temperature increases is qualitatively different from the behavior obtained at $pO_2=2\times10^{-4}$ and 1×10^{-5} atm. While at $pO_2=10^{-3}$ atm the oxygen content of the sample shows a constant slope with increasing T, at $pO_2=2\times10^{-4}$ and 1×10^{-5} atm the isobars show a region where a small increase of temperature produces a significant change in the oxygen content of the sample. These regions are indicated as A–A′ and B–B′ in Fig. 3. This behavior suggests a discontinuity of the oxygen content as a function of T

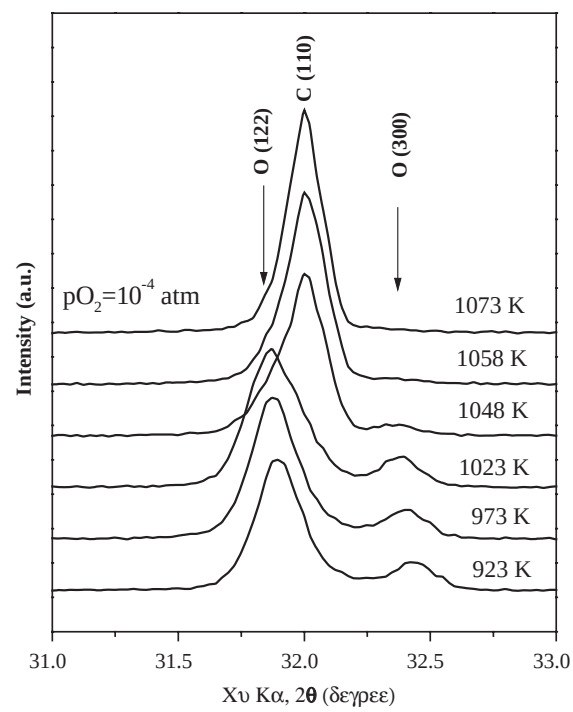

Fig. 4. X-ray diffraction data of $Sr_2Co_{1.6}Fe_{0.4}O_5$ showing the 2θ region $31\leqslant 2\theta\leqslant 33$ to follow the orthorhombic to cubic phase transition with temperature. Patterns were recorded at constant $pO_2=10^{-4}$ atm.

that can be associated to the presence of a two-phase field (C + O).

To support the presence of the two-phase field detected from isobaric measurements we have studied the evolution of the crystal structure as a function of T under constant pO_2 by HTXRD. Fig. 4 shows the variation of X-ray diffraction data of the O phase with temperature in the 2θ region $31<2\theta<33°$ obtained under $pO_2=10^{-4}$ atm. The orthorhombic phase is stable until $T=973$ K. At $T=1023$ K the width of the peak

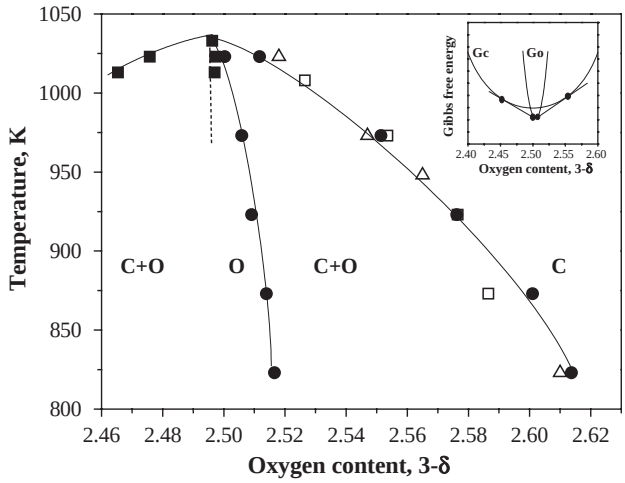

Fig. 5. Phase diagram of $SrCo_{0.8}Fe_{0.2}O_{3-\delta}$. Experimental data from (•) isothermal measurements, (■) isobaric measurements, (△) Ref. [11], and (□) Ref. [16]. The inset shows the schematic free energy–composition curves for the cubic and orthorhombic phases at a given T lower than 1023 K.

(1 2 2) of the O phase increases due to the (1 1 0) reflection of the cubic phase begins to grow. Both phases coexist at $T = 1023$ and 1048 K though the orthorhombic phase could not be detected at $T = 1058$ K. This observation is in good agreement with the data plotted in Fig. 3 where a substantial change in the oxygen content occurs from $T = 1025$ to 1050 K indicating the coexistence of both phases.

Fig. 5 shows the $T-(3-\delta)$ phase diagram determined from the isotherms and isobars described above. The (C + O)/C and the O/(C + O) (•) phase boundaries at the rich oxygen side were determined from isothermal measurements, while the (C + O)/O and the C/(C + O) phase boundaries at the poor oxygen side were obtained from isobaric measurements (■). Literature data corresponding to the phase boundary (C + O)/C of the $SrCo_{0.8}Fe_{0.2}O_{3-\delta}$ compound [11,16] were also included in Fig. 5 revealing a good agreement with our results.

In the inset of Fig. 5 we have drawn schematically the free energy–composition curves for the cubic and orthorhombic phases at a given T lower than 1023 K. The cubic phase is represented by a broad free energy function while that corresponding to the orthorhombic phase displays a narrow range of oxygen non-stoichiometry. The common tangents between the C and the O phases define the boundaries of each region in the temperature-composition phase diagram of Fig. 5.

3.2. Partial molar thermodynamic properties of the cubic phase

In thermodynamic equilibrium the oxygen chemical potential of the oxide is equal to that of the gas surrounding the sample and can be expressed as a

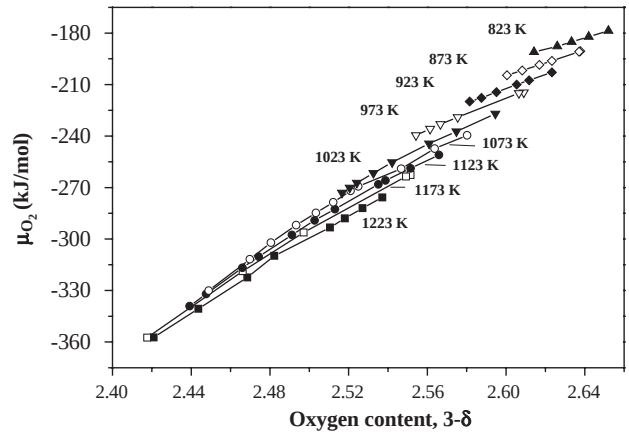

Fig. 6. Oxygen chemical potential of $SrCo_{0.8}Fe_{0.2}O_{3-\delta}$ as a function of the oxygen content at various temperatures.

function of the pO_2 of the gas by the relation:

$$\mu_{O_2}^{oxide} = \mu_{O_2}^{gas} = \mu_{O_2}^{ref} + RT\ln(pO_2/pO_2^{ref}), \quad (1)$$

where R is the gas constant and $pO_2^{ref} = 1$ atm, $\mu_{O_2}^{ref}$ the oxygen chemical potential of the reference gas and is given in tables [22]. The variation of $\mu_{O_2}^{oxide}$ with the oxygen content at various temperatures for the cubic phase has been computed from thermogravimetric data (see Fig. 2) and is shown in Fig. 6. Unlike the perovskite phases $La_{1-x}Sr_xCoO_3$ with $x = 0.2$, 0.4 and 0.7 [23] where $\mu_{O_2}^{oxide}$ shows little dependence on temperature, the data obtained for the cubic phase indicate that $\mu_{O_2}^{oxide}$ varies with temperature especially for δ values lower than 0.5. The thermodynamic quantities $h_{O_2}^{oxide}$ and $s_{O_2}^{oxide}$ were computed from $\mu_{O_2}^{oxide}$data shown in Fig. 6 using the following relations:

$$s_{O_2}^{oxide} = -\frac{\partial \mu_{O_2}^{oxide}}{\partial T}|_{\delta}, \quad (2)$$

$$h_{O_2}^{oxide} = \frac{\partial(\mu_{O_2}^{oxide}/T)}{\partial(1/T)}|_{\delta}. \quad (3)$$

The results are displayed in Fig. 7 as a function of the oxygen non-stoichiometry. Both $h_{O_2}^{oxide}$ and $s_{O_2}^{oxide}$ decrease with increasing oxygen non-stoichiometry, which agrees with $s_{O_2}^{oxide}$ data computed by us from experimental data of Liu et al. [11]. However, the variation of $s_{O_2}^{oxide}$ with the oxygen non-stoichiometry for $SrCo_{0.8}Fe_{0.2}O_{3-\delta}$ contrasts with the behavior observed for other perovskite phases such us $La_{1-x}Sr_xCoO_{3-\delta}$ with $0 \leqslant x \leqslant 0.7$ where $s_{O_2}^{oxide}$ increases with δ [23,24]. The oxygen vacancy concentration range of these perovskite phases [24] is lower than the oxygen non-stoichiometry observed for $SrCo_{0.8}Fe_{0.2}O_{3-\delta}$, which allows the application of the ideal solution model to explain the dependence of the $s_{O_2}^{oxide}$ with δ, as was discussed by Mizusaki et al. [24]. In our case, due to the high oxygen vacancy concentration, the electrostatic interactions between oxygen defects could lead to the formation of

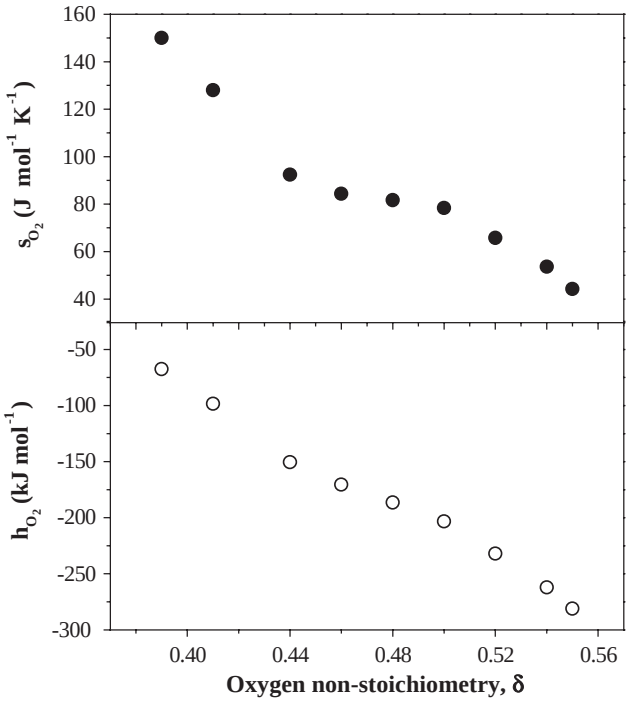

Fig. 7. Plots of $s_{O_2}^{oxide}$ and $h_{O_2}^{oxide}$ as a function of the oxygen content for $SrCo_{0.8}Fe_{0.2}O_{3-\delta}$.

ordered regions such as clusters or microdomains at temperatures above that of the order transition. Thus, the configurational entropy $S^{conf} = R \ln W$ would decrease with respect to that of the ideal solution causing the observed dependence of $s_{O_2}^{oxide}$ on δ for the cubic phase.

3.3. Electrical conductivity measurements

Fig. 8 shows the variation of the electrical conductivity σ with temperature on the low oxygen content side of the phase diagram ($\delta \geqslant 0.5$) of $SrCo_{0.8}Fe_{0.2}O_{3-\delta}$ for three different values of pO_2. The electrical conductivity increases with increasing temperature in the temperature range $800 \leqslant T \leqslant 1000$ K where the orthorhombic brownmillerite phase is stable. This result indicates that the charge carrier transport mechanism for the O phase is thermally activated. Under atmospheres with different pO_2 values, the oxygen content of the O phase stays practically constant at $3-\delta \approx 2.5$ causing small variations of the electrical conductivity at a given temperature. The inset of Fig. 8 shows the variation of the electrical conductivity with temperature for the O phase in Arrhenius coordinates. The activation energy of the thermally activated conduction mechanism has been estimated from the slope of the curve $\ln \sigma T$ vs. $10^3/T$. The obtained value was $E_o = 0.17$ eV. At $T \approx 1000$ K the electrical conductivity reaches a maximum and then decreases with increasing temperature revealing the O to C phase transition. The variation of the electrical conductivity with temperature of the C phase at

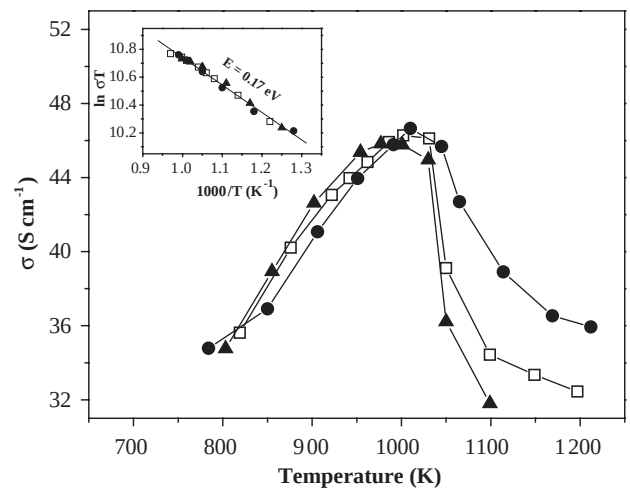

Fig. 8. Variation of σ with temperature at constant pO_2 at the low oxygen content side of the phase diagram of $SrCo_{0.8}Fe_{0.2}O_{3-\delta}$. (•) $pO_2 = 8.8 \times 10^{-4}$ atm, (□) $pO_2 = 2 \times 10^{-4}$ atm, (▲) $pO_2 = 7.5 \times 10^{-5}$ atm. The inset shows the electrical conductivity data corresponding to the brownmillerite phase in Arrhenius coordinates.

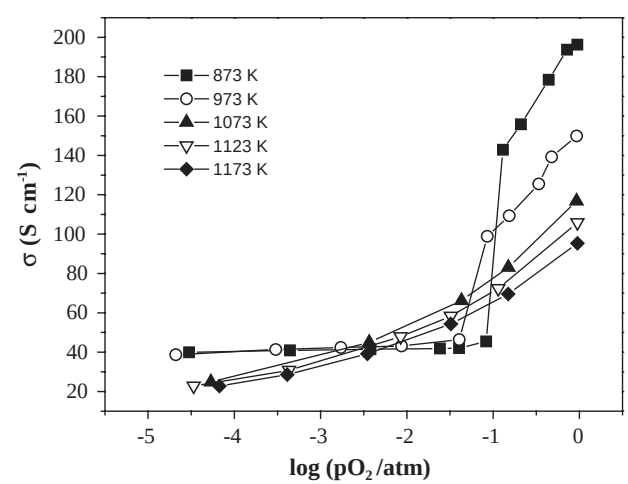

Fig. 9. Isothermal variation of σ with the equilibrium pO_2 for $SrCo_{0.8}Fe_{0.2}O_{3-\delta}$ for various temperatures.

$T \geqslant 1000$ K and constant pO_2 reflects the lowering of the oxygen content of the sample with increasing temperature and therefore a reduction of the charge carrier concentration rather than a metallic behavior. In fact, it will be shown below (see Fig. 11) that the conductivity of the C phase increases as T increases at constant oxygen content values revealing a thermally activated conduction mechanism for the C phase.

Fig. 9 displays the isotherms of σ as a function of pO_2 for the temperature range $873 \leqslant T \leqslant 1173$. In agreement with the thermogravimetric data of Fig. 2, σ exhibits a monotonic behavior for $T \geqslant 1073$ K in the pO_2 range where the cubic phase is stable. The presence of a plateau in the isotherms for $T \leqslant 973$ K shows the coexistence of the C and O phases.

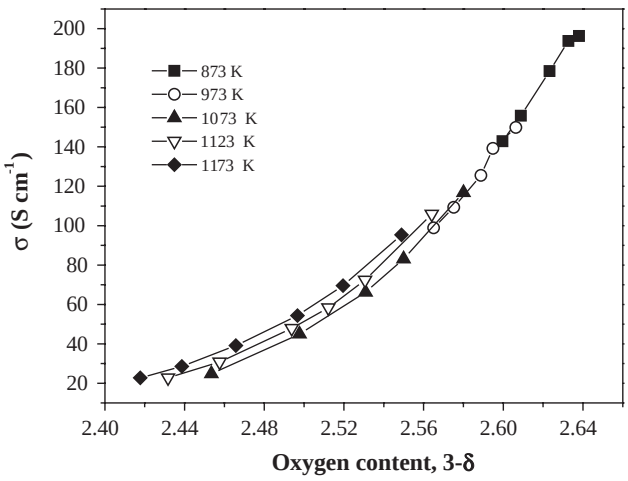

Fig. 10. Plots of σ as a function of the oxygen content for $SrCo_{0.8}Fe_{0.2}O_{3-\delta}$ at various temperatures.

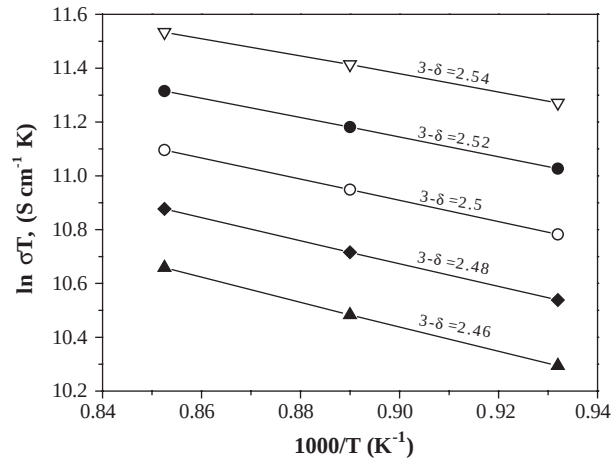

Fig. 11. Arrhenius plots of the variation of electrical conductivity of the cubic phase with inverse temperature at different oxygen content values.

The variation of the electrical conductivity with oxygen content at several temperatures for the C phase was calculated from the $\log(pO_2/\text{atm})$ vs. δ and σ vs. $\log(pO_2/\text{atm})$ curves and is shown in Fig. 10. The electrical conductivity increases with the oxygen content "$3-\delta$". The dependence is non-linear and similar to that reported for $La_{0.6}Sr_{0.4}CoO_{3-\delta}$ [25]. The behavior of the electrical conductivity of $La_{0.6}Sr_{0.4}CoO_{3-\delta}$ was analyzed in the frame of the small polaron model [25] described by the formula

$$\sigma = A\frac{e^2a^2\nu_0}{kT}e^{-E/kT} = \frac{B}{T}e^{-E/kT}, \tag{4}$$

where E is the hopping energy, e the electronic charge, a the intersite distance (~ 3.8 Å), k the Boltzmann's constant and ν_0 the vibration frequency for optical phonons. The factor A is related to the site fraction of electron holes and gives the probability that neighboring species have the appropriate charge to transfer the polaron.

To determine the activation energy associated with the polaron mechanism it is necessary to study the behavior of the electrical conductivity with temperature at constant oxygen content. In Fig. 11 we show $\ln(\sigma T)$ vs. $10^3/T$ data corresponding to the cubic phase at a fixed oxygen content obtained from those plotted in Fig. 10. The hopping energy for each oxygen content value was estimated from the slope of the straight lines used to fit the experimental data. It is found that the activation energy decreases from 0.4 to 0.28 eV with increasing oxygen content (carrier concentration) from 2.46 to 2.54, which is also consistent with small polaron theory. Mott [26] showed that the increase of polaron concentration produces an overlap of the polarization clouds with the consequent reduction of the energy required for hopping.

The electrical conductivity of the cubic phase for an oxygen content close to $3-\delta = 2.5$ compared with that of the orthorhombic one shows activation energy values ($E_c \sim 0.34$ eV) clearly higher than the value determined for the orthorhombic phase ($E_o = 0.17$ eV). This result also correlates with the higher electrical conductivity of the O phase relative to that of the disordered C phase. These differences in the charge carrier transport behavior suggest differences in their respective electronic structures due to changes in both the crystalline structure and the oxidation state of the metal transition ions participating in the transport process. The similarities observed in the variation of the electrical conductivity with the oxygen content between $SrCo_{0.8}Fe_{0.2}O_{3-\delta}$ and $La_{0.3}Sr_{0.6}CoO_{3-\delta}$ [25] suggest that the polaron mechanism may involve the jump of a hole from the HS Co^{4+} to the t_{2g} electron of the HS Co^{3+}. However, due to the presence of iron and the difficulty of stabilizing Co^{4+} compared to Fe^{4+}, more experimental evidence is needed in order to elucidate which ions participate in the polaron transport mechanism of the $SrCo_{0.8}Fe_{0.2}O_{3-\delta}$ compound.

4. Conclusions

The $T-(3-\delta)$ phase diagram of the compound $SrCo_{0.8}Fe_{0.2}O_{3-\delta}$ has been reviewed and determined in more detail for the oxygen content range $2.46 \leqslant 3-\delta \leqslant 2.6$. While the brownmillerite phase stabilizes at temperatures below 1073 K and exhibits a narrow stability range around $3-\delta \sim 2.5$, the cubic perovskite phase displays a broad range of oxygen non-stoichiometry between 2.46 and 2.6. For $T < 1073$ K, the cubic phase is separated from the orthorhombic phase by two phase regions at both sides of the orthorhombic phase. Chemical hysteresis was

observed at the perovskite to brownmillerite transition during the reduction/oxidation of $SrCo_{0.8}Fe_{0.2}O_{3-\delta}$ under isothermal conditions. The amplitude in pO_2 of the hysteresis loop decreases with decreasing temperature. We propose that coherent intergrowth with elastic strain energy between both phases is the origin of the chemical hysteresis. The negative variation of the partial molar properties $h_{O_2}^{oxide}$ and $s_{O_2}^{oxide}$ with the oxygen non-stoichiometry is explained considering the formation of ordered microdomains in the cubic phase. The electrical conductivity (σ) behavior of the cubic phase at high temperature was analyzed in the frame of the small polaron model.

Acknowledgments

We gratefully acknowledge Dr. J. Fouletier for useful discussions and the help of V. Grünfeld in the English revision of this manuscript. This work was supported by CNEA (Argentine Research Commission), Fundación Antorchas (Argentina) and Cooperation Program ECOS-SUD.

References

[1] Y. Teraoka, H. Zhang, S. Furukawa, N. Yamazoe, Chem. Lett. (1985) 1743–1746.
[2] Y. Teraoka, H. Zhang, K. Okamoto, N. Yamazoe, Mater. Res. Bull. 23 (1988) 51–58.
[3] L. Qiu, T.H. Lee, L.-M. Liu, Y.L. Yang, A.J. Jacobson, Solid State Ionics 76 (1995) 321–329.
[4] H. Kruidhof, H.J.M. Bowmeester, R.H.E.v. Doorn, A.J. Burggraaf, Solid State Ionics 63–65 (1995) 816–822.
[5] S.J. Skinner, Int. J. Inorg. Mater. 3 (2001) 113–121.
[6] H.J. Bouwmeester, A.J. Burggraaf, in: P.J. Gellings, H.J. Bouwmeester (Eds.), The CRC Handbook of Solid State Electrochemistry, CRC Press, Boca Raton, FL, 1997 (Chapter 14).
[7] U. Balachandran, J.T. Dusek, S.M. Sweeney, R.B. Poeppel, R.L. Mieville, P.S. Maiya, M.S. Kleefisch, S. Pei, T.P. Kobylinski, C.A. Udovich, A.C. Bose, Am. Ceramic Soc. Bull. 74 (1995) 71–75.
[8] F. Prado, T. Armstrong, A. Caneiro, A. Manthiram, J. Electrochem. Soc. 148 (2001) J7–J14.
[9] J. Rodriguez, J.M. Gonzalez-Calbet, J.C. Grenier, J. Pannetier, M. Anne, Solid State Commun. 62 (1987) 231–234.
[10] W.T. Harrison, T.H. Lee, Y.L. Yang, D.P. Scarfe, L.M. Liu, A.J. Jacobson, Mater. Res. Bull. 30 (1995) 621–630.
[11] L.M. Liu, T.H. Lee, L. Qiu, Y.L. Yang, A.J. Jacobson, Mater. Res. Bull. 31 (1996) 29–35.
[12] J.P. Hodges, S. Short, J.D. Jorgensen, J. Solid State Chem. 151 (2000) 190–209.
[13] S. Pei, M.S. Kleefisch, T.P. Kobylinski, J. Faber, C.A. Udovich, V. Zhang-McCoy, B. Dabrowski, U. Balachandran, R.L. Mieville, R.B. Poeppel, Catal. Lett. 30 (1995) 201–212.
[14] K. Huang, J. Wang, J.B. Goodenough, J. Mater. Sci. 36 (2001) 1093–1098.
[15] V.N. Tikhonovich, O.M. Zharkovskaya, E.N. Naumovich, I.A. Bashmakov, V.V. Kharton, A.A. Vecher, Solid State Ionics 160 (2003) 259–270.
[16] V.N. Tikhonovich, E.N. Naumovich, D.I. Logvinovich, V.V. Kharton, A.A. Vecher, J. Solid State Electrochem. 7 (2003) 77–82.
[17] A. Caneiro, M. Bonnat, J. Fouletier, J. Appl. Electrochem. 11 (1981) 83–90.
[18] A. Caneiro, P. Bavdaz, J. Fouletier, J.P. Abriata, Rev. Sci. Instrum. 53 (1982) 1072–1075.
[19] D.R. Knittel, S.P. Pack, S.H. Lin, L. Eyring, J. Chem. Phys. 67 (1977) 134–142.
[20] H. Inaba, S.P. Pack, S.H. Lin, L. Eyring, J. Solid State Chem. 33 (1980) 295–304.
[21] D.A. Porter, K.E. Easterling, Phase Transformations in Metals and Alloys, Chapman & Hall, London, 1991.
[22] IUPAC, Commission on Thermodynamics, "Oxygen, International Thermodynamic Tables of the Fluid State –9," Blackwell Scientific, Oxford, 1987.
[23] M.H.R. Lankhorst, H.J.M. Bouwmeester, H. Verweij, J. Solid State Chem. 133 (1997) 555–567.
[24] J. Mizusaki, Y. Mima, S. Yamauchi, K. Fueki, H. Tawaga, J. Solid State Chem. 80 (1989) 102–111.
[25] E.B. Mitberg, M.V. Patrakeev, I.A. Leonidov, V.L. Kozhevnikov, K.R. Poeppelmeier, Solid State Ionics 130 (2000) 325–330.
[26] N.F. Mott, Metal–Insulator Transitions, 2nd edition, Taylor & Francis, London, 1974.